Optical Materials 138 (2023) 113657

Contents lists available at ScienceDirect

Optical Materials

journal homepage: www.elsevier.com/locate/optmat

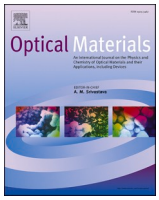

Research Article

Influence of embedded NiO-nanoparticles on the nonlinear absorption of tungsten disulfide nanolayers

Srinivasa Rao Konda [a,*], Rahul A. Rajan [a,b], Subhash Singh [a,c], Rashid A. Ganeev [a,d,e,f], Venugopal Rao Soma [g], Amit Srivastava [h], Mottamchetty Venkatesh [a,i], Chunlei Guo [c], Wei Li [a,**]

[a] The GPL Photonics Laboratory, State Key Laboratory of Luminescence and Applications, Changchun Institute of Optics, Fine Mechanics and Physics, Chinese Academy of Sciences, Changchun, Jilin, 130033, China
[b] University of Chinese Academy of Sciences Beijing, 100049, PR China
[c] The Institute of Optics, University of Rochester, Rochester, NY, 14627, USA
[d] Laboratory of Nonlinear Optics, University of Latvia, Riga, LV-1586, Latvia
[e] Tashkent Institute of Irrigation and Agricultural Mechanization Engineers, National Research University, Kori Niyozov street 39, Tashkent, 100000, Uzbekistan
[f] Department of Physics, Voronezh State University, Voronezh, 394006, Russia
[g] Advanced Center of Research in High Energy Materials (ACRHEM), DRDO Industry Academia - Centre of Excellence (DIA-COE), University of Hyderabad, Hyderabad, 500046, Telangana, India
[h] Department of Physics, TDPG College, VBS Purvanchal University, Jaunpur, 222001, India
[i] Department of Materials Science and Engineering, Uppsala University, Box 35, SE-75103, Uppsala, Sweden

ARTICLE INFO

Keywords:
WS_2
NiO nanoparticles
Nonlinear absorption
Nonlinear refraction

ABSTRACT

2D transition metal dichalcogenides possess fascinating properties due to their direct bandgap, strong spin-orbit coupling, and promising electronic/mechanical properties. In this work, we synthesized pure tungsten disulfide (WS_2) nanolayers and NiO nanoparticles (NPs) decorated in few-layered WS_2 and measured the third-order nonlinear optical properties using femtosecond Z-scan measurements. The open aperture Z-scan data illustrated that the inclusion of NiO nanoparticles into the WS_2 layers increases the nonlinear absorption at 800 and 400 nm wavelengths. Furthermore, we observed the switchability of the nonlinear absorption from saturable absorption to two-photon absorption or reverse saturable absorption by changing the pump intensity. Thus, the embedded NiO NPs played a crucial role in the variation of intensity-dependent nonlinear absorption mechanism of WS_2 nanolayers and thus can be helpful for various optical applications such as laser pulse compression and optical limiting to prevent over-exposure of protective photosensitive sensors by intense ultrashort laser pulses.

1. Introduction

Materials displaying excellent third-order nonlinear optical (NLO) responses upon intense and ultrashort laser pulses excitation find applications in different areas of photonics. The responses are gauged through variations in the nonlinear absorption and refraction with respect to the incident beam intensity. The saturable absorbers (SA) are suitable aspirants for optical devices such as Q-switches and mode-locking devices [1,2]. A few of the previous studies proposed that nanomaterial-based saturable absorbers exhibit enhanced performance compared to the conventional saturable absorbers [3]. Meanwhile, 2D nanomaterials not only exhibit capable saturable absorption (SA) properties [4,5], but also attain massive research attention in applications such as photoelectric conversion, energy storage, sensing, catalysis, and many other photonic applications [6–16]. Particularly, transition metal dichalcogenides (TMDs) are the hexagonal semiconductors having transition metal atoms attached by weak Wander Waals force between two layers of chalcogen atoms. 2D-TMDs represent the evolving class of materials with assets that make them extremely attractive for fundamental studies of novel physical phenomena [17–20]. These materials are very compact with some layers on a 2D atomic scale and possess direct bandgap. Therefore, they could afford a solid interface with the incident photon and possess the favorable features such as broad band absorption, transparency, and high carrier mobility.

Over the past years, there was much interest in 2D TMDs,

* Corresponding author.
** Corresponding author.
E-mail addresses: ksrao@ciomp.ac.cn (S.R. Konda), weili1@ciomp.ac.cn (W. Li).

https://doi.org/10.1016/j.optmat.2023.113657
Received 13 December 2022; Received in revised form 8 February 2023; Accepted 3 March 2023
Available online 8 March 2023
0925-3467/© 2023 Elsevier B.V. All rights reserved.

particularly MoS_2 monolayers that are well explored in various applications [20–27]. WS_2 nanolayers also belongs to this category. The bandgap of such materials depends on the number of layers and the type of dopants. Examining the modified morphological, linear, and third-order NLO properties of 2D TMDs like WS_2 nanolayers is a significant research topic as they can be utilized in evolving next-generation high-performance optical devices [28–30]. A few research groups explored the NLO properties of WS_2 thin films of various thickness using different excitation wavelengths. They demonstrated that the nonlinear absorption mechanism significantly depends on the laser pump intensity and excitation wavelength [19,31–33]. WS_2, MoS_2, and $MoSe_2$ are classified as hexagonal semiconductors comprising transition metal atoms that are packed between two layers of chalcogen atoms. These layers of chalcogen atoms are attached using a weak Vander Waals forces [32]. Interestingly, the bulk TMDs usually revealed indirect bandgap, whereas their monolayer/thin-film counterparts illustrate a direct bandgap. Recently, Stavrou et al. demonstrated the control of the crystalline phase of MoS_2 and WS_2, which provides an efficient strategy for 2D nanostructures with custom-made NLO properties for specific optoelectronic and photonic applications [34,35]. These materials possess diverse NLO properties and can be tailored easily by simply changing the chalcogen atom.

In present work, we analyzed the aqueous solutions of WS_2 and NiO nanoparticles (NPs) decorated few-layered WS_2 nanosheets (here after referred as Ni-WS_2) and investigated their NLO properties using the femtosecond Z-scan technique at two wavelengths (800 and 400 nm). We demonstrated that the Ni dopants play a pivotal role in the nonlinear absorption of WS_2. Results shows that the nonlinear absorption of such structures is influenced by the wavelength and intensity of laser radiation. Our work undoubtedly reveals the advantages of embedded NiO nanoparticles on WS_2 layers for potential applications in optical devices.

2. Materials and methods

2.1. Materials

All the chemicals used for this study such as N-dimethylformamide (DMF), nickel acetate (Ni $(CH_3CO_2)_2{\cdot}2H_2O$), sodium hydroxide (NaOH), and sulphuric acid (H_2SO_4) were of analytical grade provided by Sigma-Aldrich. All these reactants and solvents were used as received without any post processing. We used deionized water and ultrapure double distilled water for the preparation of the aqueous solutions, when required.

2.2. Synthesis of nickel oxide NPs

Nickel oxide NPs were produced by chemically reducing nickel acetate with polyethylene glycol as a stabilizing agent. In this synthesis procedure, as a first step, we mixed 1 M aqueous solution of nickel acetate with polyethylene glycol for 60 min while continuously stirring. A 1 M NaOH aqueous solution was filled into a burette tube in the vertical column and dispensed drop by drop into the nickel acetate/PEG mixture while continuously stirring. The resulting solution was then centrifuged at 5000 rpm for 10 min with 200 ml of deionized water before being stored in a glass vial for later use.

2.3. Synthesis of few-layer WS_2 and NiO nanoparticles decorated WS_2

Few-layer WS_2 nanosheet sample was created by mechanically exfoliating bulk WS_2 powder (purity 99.999% Sigma Aldrich) in dimethyl formamide (DMF) solvent using a pressurized ultrasonic reactor. In brief, 50 mg WS_2 powder was suspended in 500 ml DMF and exfoliated for 10 h using intense ultrasonication. 2 ml of the supernatant of NiO NPs was added to the WS_2/DMF solution and exfoliated for another 10 h. Finally, the prepared solutions were filtered through 0.22 μm porous filter membranes and washed several times with deionized water. The final sample was vacuum dried for 12 h at 80 °C before being stored in cleaned airtight glass containers for further characterization and application.

2.4. Characterization: UV–visible, XRD, Raman, and SEM instrumental details

The powder samples were initially dissolved in double-distilled water and their UV–visible absorption spectra were further measured using PerkinElmer Lambda 365 double-beam spectrophotometer. The powder samples were exposed to X-ray diffraction (PANalytical X'Pert PRO X-ray diffractometer; with CuKα radiation source $\lambda = 1.54178$ Å) for diagnosing crystallinity and phase of samples between 2θ range of 10-80°. Raman spectroscopic measurements were carried out using Renishaw Invia micro-Raman spectrometer with 584 nm excitation line from Are Kr laser. A 100 × objective lens focused the laser beam on the sample surface and the backscattered Raman signal was collected with 10 s accumulation time. The surface morphology of samples was confirmed by scanning electron microscopy (FEI Nova 400, operated at 20 kV).

2.5. Z-scan measurements

The fundamental (800 nm) and its second harmonic wavelengths (400 nm) were used for measuring the third-order nonlinearities of the studied samples. A Ti: sapphire laser system (M/s Spectra-Physics, Spitfire Ace) operating at 800 nm, 35 fs, 1 kHz. The 400 nm was obtained from 800 nm using a type I beta-barium borate (BBO) crystal of thickness 0.2 mm, which was placed between the attenuator and focusing lens as shown in Fig. 1(b). The residual of 800 nm pulses was blocked by color filter. We have measured the pulse duration of input pulse before BBO, using a commercial autocorrelator (PulseScout2, Newport) which was approximately 60 fs, ($\tau_{fs} = \tau_{auto}/\sqrt{2}$). However, we did not measure the pulse duration after the BBO, which required additional method (Cross-correlation) for 400 nm. We do not have this set up for measurement in our lab. Meanwhile, as per the specifications of BBO and 0.2 mm thickness might broaden the pulse duration to 65–70 fs. Therefore, the extended pulse duration leads to very small variation in the laser peak intensity, which falls in the experimental errors of the provided Z-scan data. The spectral profiles of fundamental and second harmonic were measured using a USB spectrometer. A 400 nm spherical lens focused the laser pulses and the focus spot had $1/e^2$ beam radius $w_0 = 38.5$ μm. The 800 nm laser pulse energy was controlled by an attenuator. For measuring the nonlinear absorption coefficients (β), saturation intensities (I_{sat}) and nonlinear refractive indices (n_2) in the case of open-aperture (OA) and closed-aperture (CA) measurements, we used four different energies (100, 280, 350 and 400 nJ; the corresponding peak intensities $I_{800\ nm}$ were 67, 188, 235 and 269 GW/cm^2). In the case of 400 nm pulses, we used 30,50, 100 and 280 nJ pulse energies ($I_{400\ nm}$ = 20, 33, 67 and 188 GW/cm^2). The 5 mg of powdered sample was dispersed in double-distilled water and made for ultrasonication for up to 15 min. The measured concentrations of the WS_2 and Ni-WS_2 were found to be to 6.8×10^{-14} mol/L and 5.5×10^{-4} mol/L, respectively. The aqueous solution was filled in 1 mm quartz cuvette placed on the translation stage and moved along the Z-scan path. At each point, the laser pulses were collected by photodiodes 1 and 2 for open- and closed-aperture Z-scan measurements, as shown in Fig. 1(b).

3. Results and discussion

3.1. Surface morphology, UV–visible absorption, and phase and crystallinity of samples

SEM images of pristine (WS_2) and Ni-WS_2 nanosheets are presented in Fig. 1(c–f). Pristine WS_2 nanoflakes get assembled into 3D space to form free-standing mostly hexagonal shapes stacked together [Fig. 1(c

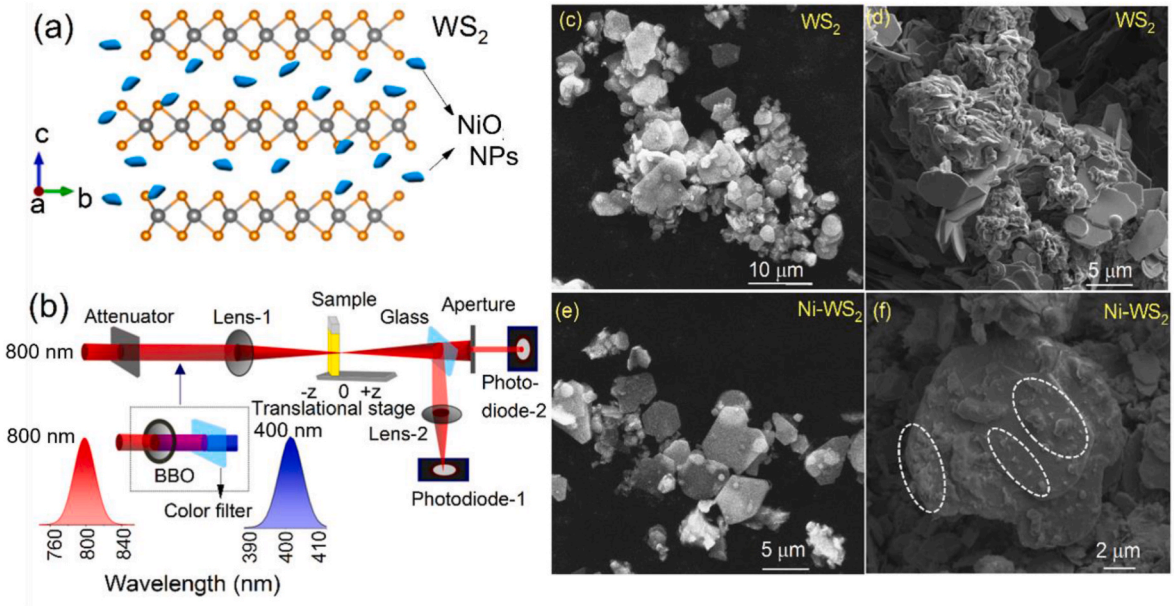

Fig. 1. (a) Schematic of few-layer WS_2/NiO NPs nanocomposite. (b) Z-scan experimental setup. Lens-1 (f = 400 nm). The laser pulse spectral profiles are shown in red and blue color spectra at 800 nm and 400 nm. SEM images of (c, d) WS_2 and (e, f) Ni-WS_2 at two different positions, in which some traces of NiO nanoparticles deposited on the WS_2 are marked by white dotted lines.

and d)]. The thickness of each shape was in the range of 1–2 μm. The embedded NiO NPs changed the morphology of as-created WS_2 nanosheets and were attached on the top of WS_2 layers, which are visible in Fig. 1(e and f). Earlier the similar NiO NPs were embedded in MoS_2 layers, where we have shown the SEM and TEM images for this NiO NPs embedded in MoS_2 [36]. The embedded NiO NPs having average size distribution of 20–50 nm, which are functionalized on the surface of WS_2 nanoflakes in the present case. The few-layered WS_2 and Ni-WS_2 were characterized using different analytical techniques for investigating their structural, chemical and optical properties.

UV–visible absorption spectra of WS_2 and Ni-WS_2 are presented in Fig. 2(a). Based on absorption spectra we measured the linear absorption coefficient (α_0) for WS_2 and Ni-WS_2, at 400 nm and 800 nm wavelengths. WS_2 having α_0 0.12 cm^{-1} at both wavelengths, whereas Ni-WS_2 possess 0.03 cm^{-1} at 800 nm and 0.04 cm^{-1} at 400 nm. The normalized absorption spectra of pristine WS_2 few layered samples show weak excitonic peaks at 391 nm (3.17 eV) and 642 nm (1.93 eV). After the doping of NiO NPs, the absorption peaks appeared around 648 nm (1.91 eV), 530 nm (2.33 eV), and 380 nm (3.26 eV), which are labeled as “A”, “B”, and “C”, respectively [37,38]. Peaks “A” and “B” are associated with the excitonic absorption of the direct gap located at the K-point in the Brillouin zone [39], and peak “C” resulted from the transitions between

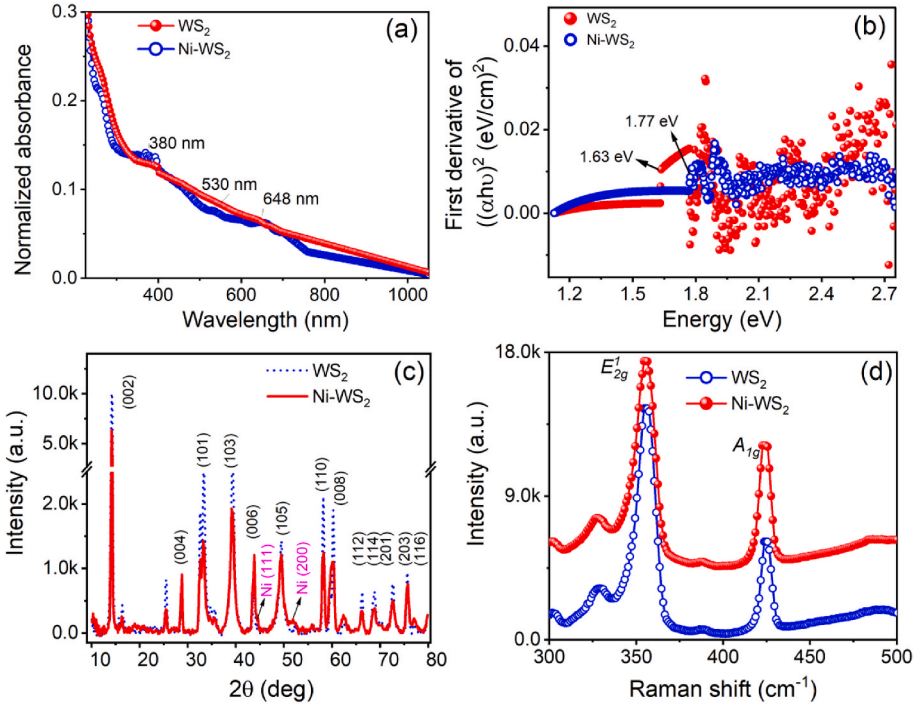

Fig. 2. (a) UV–visible absorption spectra and (b) corresponding d$((\alpha h\nu)^2)$/d $(h\nu)$ curve of WS_2 and Ni-WS_2, (c) XRD, (d) Raman spectra of WS_2 and Ni-WS_2.

the density of state peaks belongs to the valence and conduction bands [40]. Noticeably, after the doping of NiO NPs, the excitonic peak B becomes prominent and the peak "A" shows a slight blue shift. This blue shift indicates the widening of the corresponding energy band-gap, which might be resulted from the quantum confinement effect introduced by the NiO NPs along with the smaller few-layered WS_2 nano-sheets from the lateral directions [36,40]. In other words, the doping of NiO NPs with the few-layered WS_2 results in a blue shift and increase the strength of the excitonic pairs in a direct band gap because of the following possible reasons: (1) the presence of NiO NPs could form smaller sized flakes of WS_2 (2) NiO NPs disturb the electronic energy level belongs to the top of the valance band and/or bottom of the conduction band.

The absorption coefficient (α) of the samples and the bandgap energy (E_g) are related by $(\alpha h\nu)^n = A(h\nu - E_g)$, where h denotes Planck's constant, ν denotes the photon frequency, and A is a constant. The value of exponent n denotes the nature of electronic transition in the material. We can use n = 2 for direct allowed transitions, n = 2/3 for direct forbidden transition, n = 1/2 for indirectly allowed transitions, and n = 1/3 for indirect forbidden transitions. WS_2 is generally recognized as a direct bandgap material.

We have analyzed the derivative of $\ln(\alpha h\nu) = n\ln A(h\nu - E_g)$ based on the equation $\frac{d(\alpha h\nu)^2}{d(h\nu)} = \frac{n}{(h\nu - E_g)}$. The divergence observed in the plot of $\frac{d(\alpha h\nu)^2}{d(h\nu)}$ versus $h\nu$ gives the bandgap E_g, which corresponds to the electronic transition in WS_2 and Ni-WS_2 [see Fig. 2(b)]. This method can provide better accuracy in determining the bandgap energy as compared to the other methods such as the Tauc plot. The measured bandgap energy for pristine few-layered WS_2 is 1.63 eV (Fig. 2 (b)), which is higher than the direct bandgap of bulk WS_2 (1.4 eV) and smaller than the direct bandgap of monolayer WS_2 (1.905 eV) [41,42]. However, the calculated bandgap for Ni-WS_2 increased to 1.77 eV than pure WS_2 (1.63 eV). It seems that Ni doping slightly increased the bandgap of the sample, which can be attributed either due to i) the formation of lesser sized flakes in the existence of NiO NPs or (ii) NiO NPs perturb electronic energy associated with the introduction of shallow hybridized states formed with Ni-3d and S-3p states [43].

Fig. 2(c) shows the X-ray diffraction (XRD) patterns of the as-synthesized pristine WS_2 and Ni-WS_2 samples. Both the samples exhibit a dominating peak at $2\theta = 14.20^\circ$, which corresponds to the Bragg reflection from the crystalline plane of WS_2 (002). Besides, (004), (100), (101), (103), (006), (105), (110), (008), (112), (114), (201), (203) and (116) planes are identified [44], which demonstrated higher crystalline property of pristine and Ni NPs functionalized WS_2. On the other hand, the presence of Ni NPs is confirmed by identifying their dominant peaks (111) and (200). Nevertheless, XRD peaks of Ni-WS_2 have less intensity than the pristine WS_2. It might be due to reduction of the overall crystallinity of the WS_2 after incorporating the Ni NPs. There is almost no other significant difference in the two XRD signals.

Raman spectroscopy was employed to further examine the structural features of WS_2 and Ni-WS_2 samples [Fig. 2(d)]. The measurements were performed with the excitation laser wavelength at 584 nm. As illustrated in Fig. 2(d), there were two prominent optical modes, namely E^1_{2g} associated with the in-plane displacement of W and S atoms, and A_{1g} associated with the out-of-plane symmetric vibration of S atoms along the c-axis direction of the layers. The Raman peaks corresponding to Ni-WS_2 sample show a mild shift towards the lower wavenumber side. The vibrational mode A_{1g} shows a slightly higher shift (from 424.84 cm^{-1} to 424.16 cm^{-1}) than the displacement mode E^1_{2g} shift (from 355.50 cm^{-1} to 355.24 cm^{-1}). All the Raman peak positions are in very good agreement with the reported results [36,45].

3.2. Nonlinear absorption and refraction of WS_2 and Ni-WS_2 nanoflakes

In this work, we used 1 kHz pulse repetition rate pulses for performing the NLO studies of the WS_2 and Ni-WS_2 samples. In general, the thermal effect in any material is highly depends on the thermal conductivities of the material and the duration of laser pulse interaction, the latter can be directly determined based on the pulse duration and the laser repetition rate. Recent studies show that WS_2 materials exhibit high thermal conductivity of around 140 W/mK [46,47], thus the sample could rapidly dissipate the phonons generated upon laser irradiation. It should be noted that femtosecond laser irradiation creates a non-equilibrium condition between the electron and lattice system of most of the materials. Besides, the heat generated after a pulse irradiation can completely diffuse away in μs time scale [48,49], which is far less than the time delay between the adjacent laser pulses (~1 ms). The reported studies showed that the temperature accumulation from irradiation of femtosecond laser pulses is more likely to happen with a high repetition rate above 200 kHz [49–51]. Moreover, we used the pulse energy for 800 nm are 100–400 nJ and for 400 nm 30–280 nJ. The used pulse energies may not create the thermal effects on the aqueous solutions. Therefore, almost no thermal effects arise from the laser pulse irradiation on the nonlinear absorption and refraction for studied samples with 1 kHz repetition rate.

It is well recognized that Z-scan is a potential technique to measure materials' third-order NLO properties. The values of β, I_{sat}, and n_2 can be measured using the analysis of the Z-scan technique through OA and CA measurements, respectively. In the case two-photon absorption (TPA), SA, reverse saturable absorption (RSA), and combined process of SA + RSA and nonlinear refraction and absorption (NRA) the normalized transmittance of laser pulses can be described by [52–55]

$$T_{TPA}(z) = T_{RSA}(z) \approx q(z)^{-1}\ln(1+q(z)) \tag{1}$$

$$T_{SA}(z) = 1 + \frac{I_0}{I_{sat}} \times \left(x^2+1\right) \tag{2}$$

$$T_{SA+RSA}(z) = \left(q(z)^{-1}\ln(1+q(z))\right) \times \left(1 + \frac{I_0}{I_{sat}} \times \left(x^2+1\right)\right) \tag{3}$$

$$T_{NRA}(z) = 1 + \frac{2(-\rho x^2 + 2x - 3\rho)\Delta\Phi_0}{(x^2+1)(x^2+9)} \tag{4}$$

Here, $q(z) = I_0 \times \beta \times L_{eff}/(1 + z^2/(z_0)^2)$, I_0 is the peak intensity of laser pulse, $x = z/z_0$, $z_0 = kw_o^2$ is the Rayleigh length, $k = 2\pi/\lambda$ is the wavenumber, w_o is the radius of the beam waist, and $\Delta\Phi_0 = kn_2 I_0 L_{eff}$ is the phase change due to nonlinear refraction ($n_2 = \Delta\Phi_0/kL_{eff}I_0$), $L_{eff} = [1-exp(-\alpha_0 L)]/\alpha_0$ is the effective length of the nonlinear medium, α_0 is the linear absorption coefficient, L is the sample thickness. The above equations are applicable in the case of the laser beam possessing a Gaussian profile. We measured the spatial profiles of 800 nm and 400 nm beams and confirmed that those are close to the Gaussian distribution.

The third-order susceptibility ($\chi^{(3)}$), could be obtained from the real and imaginary values, which are given by

$$Re\left|\chi^{(3)}\right|(esu) = \frac{\varepsilon_0 n_0^2 c^2}{\pi} n_2 \left(\frac{m^2}{W}\right) \tag{5}$$

$$Im\left|\chi^{(3)}\right|(esu) = \frac{\varepsilon_0 n_0^2 c^2 \lambda}{4\pi^2} \beta \left(\frac{m}{W}\right) \tag{6}$$

$$\left|\chi^{(3)}\right|(esu) = \sqrt{\left[\left|Re|\chi^{(3)}|\right|^2 + \left|Im|\chi^{(3)}|\right|^2\right]^2} \tag{7}$$

Here, ε_0 is the free space permittivity (8.85×10^{-12}), n_0 is the refractive index of the solvent.

Figs. 3 and 4 show the OA and CA/OA Z-scan curves for WS_2 and Ni-WS_2 at excitation wavelengths 800 and 400 nm, respectively. The CA data divided with OA data to avoid the effect of nonlinear absorption. The nonlinear absorption coefficients, saturation intensities, and

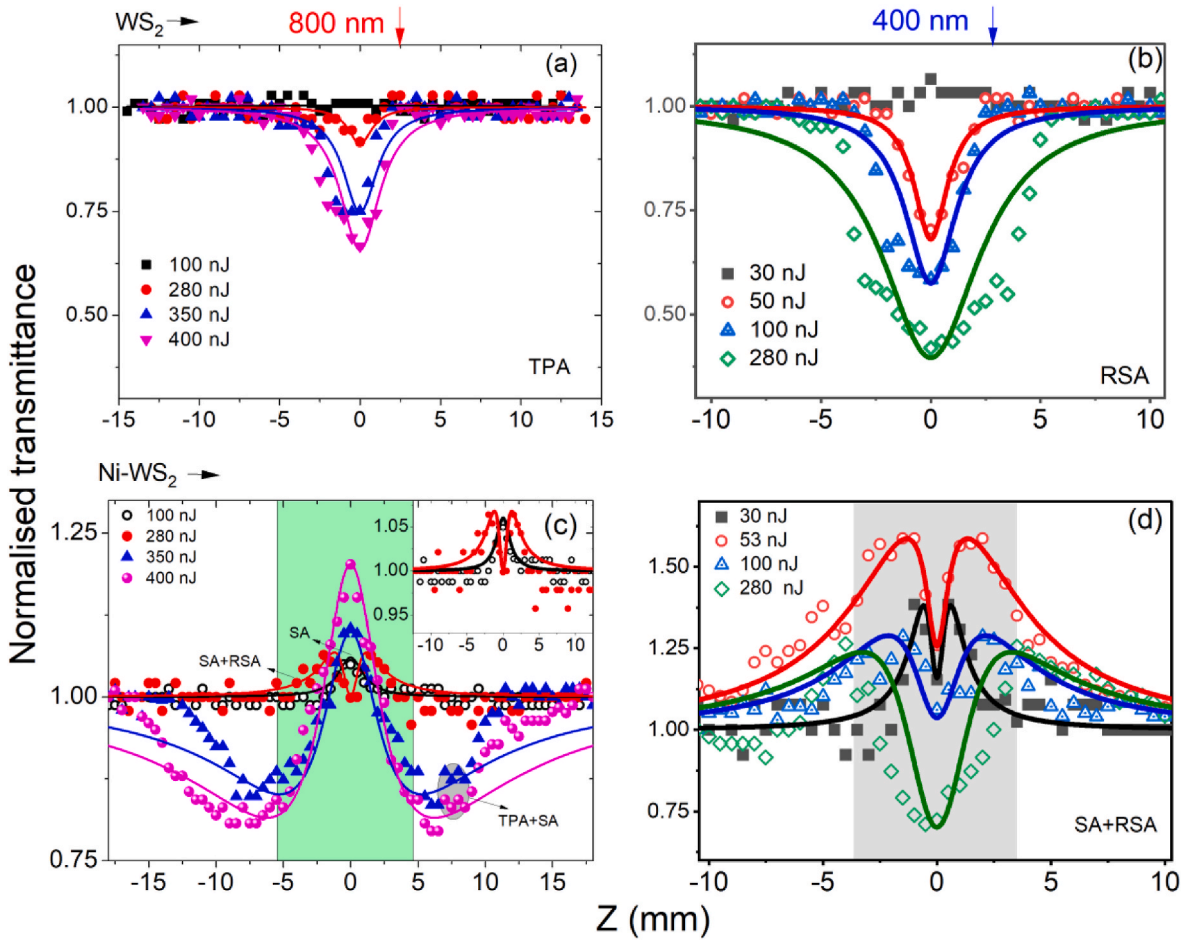

Fig. 3. Open-aperture Z-scan curves for (a) WS_2 at 800 nm, (b) WS_2 at 400 nm, (c) Ni-WS_2 at 800 nm, and (d) Ni-WS_2 at 400 nm pump wavelengths. The inset of (c) shows the zoomed Z-scans at the lower input energies (100 and 280 nJ) for better viewing of the dynamics of variations of the nonlinear optical processes. The solid lines represent theoretical fits for the corresponding absorption process using equations (1)–(3) while the symbols represent the experimental data.

nonlinear refractive indices calculated using theoretical fits [equations (1)–(4)] as well as third-order NLO susceptibility (real, and imaginary) are presented in Table 1. Almost the WS_2 having the same linear transmittance at each excitation wavelength ($\alpha_0 = 0.12$ cm^{-1}), and Ni-WS_2 having $\alpha_0 = 0.03$ and 0.04 cm^{-1} at 400 nm and 800 nm, respectively. Any way in Table 1 we compared the β/α_0 and n_2/α_0 values.

It was observed that pristine WS_2 possesses TPA and RSA at 800 and 400 nm using different laser intensities, as shown in Fig. 3(a and b), respectively. The absorption process is straightforward; there is no change of the shape of OA curve due to the influence of excitation laser pulse energy, which leads only to an increment in absorption. However, in the case of Ni-WS_2, the absorption process of 800 nm radiation is significantly switchable due to the influence of input laser energies (Fig. 3(c)). At 100 nJ (67 GW/cm^2), the sample possess SA; at 280 nJ (188 GW/cm^2), the process switches to SA + RSA ('M'-like shape of OA Z-scan curves), and at above 350 nJ (235 GW/cm^2), it shows TPA + SA ('W'-like shape of OA Z-scan curves). The embedded Ni NPs change the bandgap of the WS_2, and the pumping with 800 nm photon becomes almost equal to the bandgap of Ni-WS_2 (photon energy 1.55 eV, bandwidth of radiation: between 1.5 eV and 1.6 eV, bandgap: 1.77 eV). In general, when the bandgap of material becomes approximately equal to exciting photon energy, the primary absorption should be SA, which we observed at the lower energy (100 nJ). However, at the incident laser energy of 280 nJ, out of the focal plane we observed SA, whereas at the focal plane it was RSA, since electrons might absorb incident photons and jump to higher energy levels. Further growth of incident laser energy (350 nJ) led to TPA at lower intensities of input pulse (i.e., out of focal plane), and once sample reaches the focal plane (i.e., at high intensity) the absorption switched to the SA.

Meanwhile in the case of 400 nm, Ni-WS_2 demonstrates a combination of SA + RSA ['M' type shape curves, Fig. 3(d)] at different input energies. The excitation photon energy (3.1 eV, bandwidth of radiation: 3.08–3.11 eV) is much higher than the material's bandgap (1.77 eV). The effect on Ni dopants initially leads to SA, and at higher intensities (i.e., at focal plane) WS_2 demonstrated RSA behavior. Earlier, Jiang et al. also observed the switchable absorption process between SA + RSA to TPA + SA in the case of WS_2, ZnO films, and ZnO&WS_2 (ZnO@WS_2 and WS_2@ZnO) thin films prepared by different sputtering times (10 and 20 min) using an excitation with 800 nm, 190 fs, 1 kHz pulses [31]. They observed that for 800 nm, the WS_2 thin films (10 min and 20 min sputtering time) show TPA + SA and RSA + SA (at 50 nJ), and SA and TPA + SA (at 100 nJ), respectively.

Pristine WS_2 does not shown any absorption process at 100 nJ [Fig. 3 (a)], whereas it possesses nonlinear refraction at the same pump energy. The CA measurements (Fig. 4), shows the WS_2 and Ni-WS_2 shows the self-focusing nonlinear refraction process having the positive values of n_2. In case the WS_2 at 100 nJ for 800 nm $n_2 = 1.19 \times 10^{-15}$ cm^2/W, whereas this value slightly increased for Ni-WS_2 up to 1.47×10^{-15} cm^2/W. At other pulse energies the n_2 values for Ni-WS_2 are smaller than pure WS_2. Which is due to the influence of TPA/RSA in the case of Ni-WS_2. However, in case of 400 nm CA Z-scans, the $n_2$values slightly higher for Ni-WS_2 than WS_2 at 30 and 280 nJ pulse energies. The decrease in the β and n_2 values for Ni-WS_2 at some of the cases are explained in next paragraphs in detail by considering the ratio of normalized

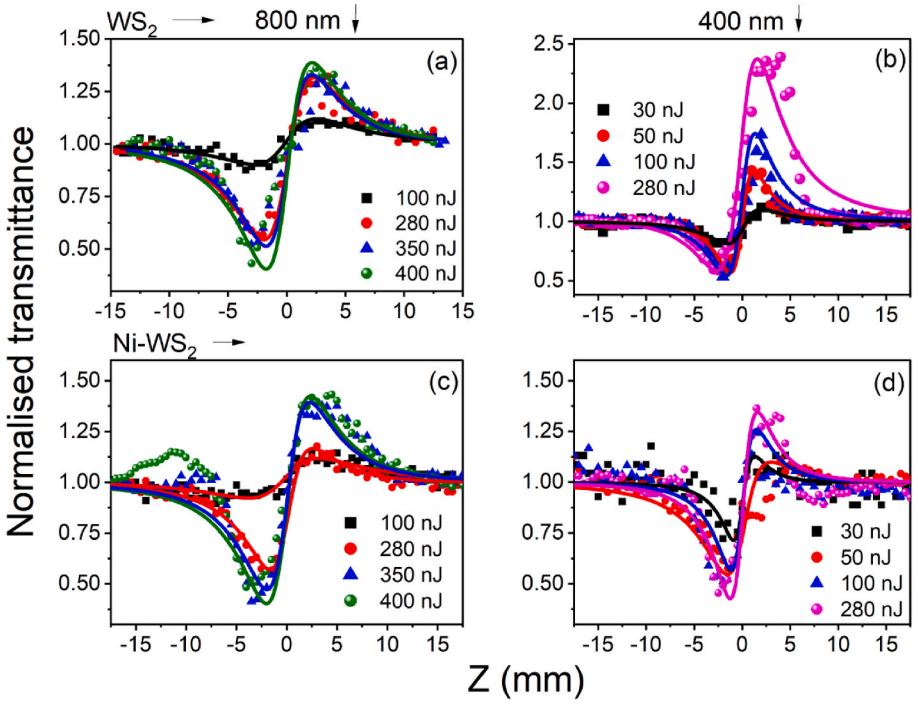

Fig. 4. The ratios of closed-aperture/open-aperture Z-scan curves for (a) WS_2 at 800 nm, (b) WS_2 at 400 nm, (c) Ni-WS_2 at 800 nm, and (d) Ni-WS_2 at 400 nm pump wavelengths. The solid lines represent theoretical fits using equation (4) while the symbols represent the experimental data.

Table 1
Nonlinear absorption coefficients (β), nonlinear refractive indices (n_2) and saturation intensities (I_{sat}), third-order nonlinear susceptibility ($\chi^{(3)}$) of WS_2 and Ni-WS_2 measured using 800 and 400 nm pulses.

Sample	Pulse energy (nJ)	Peak intensity (GW/cm^2)	Nonlinear absorption process	$\beta \times 10^{-11}$ (cm/W)	$I_{sat} \times 10^{11}$ (W/cm^2)	$n_2 \times 10^{-15}$ (cm/W^2)	$\beta/\alpha_0 \times 10^{-11}$ (cm^2/W)	$n_2/\alpha_0 \times 10^{-15}$ (cm^3/W)	Re$\lvert\chi^{(3)}\rvert \times 10^{-14}$ (esu)	Im$\lvert\chi^{(3)}\rvert \times 10^{-14}$ (esu)	$\chi^{(3)} \times 10^{-14}$ (esu)
WS_2 @800 nm	100	67				1.01 ± 0.050		8.417	4.53		4.53
	280	188	TPA	1.60 ± 0.08		1.28 ± 0.064	13.333	10.667	5.74	4.56	5.75
	350	235	TPA	3.85 ± 0.19		1.08 ± 0.054	32.083	9.000	4.84	1.09	4.96
	400	269	TPA	4.49 ± 0.22		1.13 ± 0.056	37.417	9.417	5.06	1.28	5.22
Ni-WS_2 @800 nm	100	67	SA	−2.52 ± 0.12	11.2 ± 0.56	0.91 ± 0.045		22.750	4.08	0.71	4.14
	280	188	SA + RSA	4.24 ± 0.21	2.26 ± 0.23	0.96 ± 0.048	106.000	24.000	4.30	1.21	4.47
	350	235	TPA + SA	5.58 ± 0.28	0.71 ± 0.04	1.35 ± 0.067	139.500	33.750	6.05	1.59	6.26
	400	269	TPA + SA	5.13 ± 0.26	0.59 ± 0.03	1.06 ± 0.053	128.250	26.500	4.75	1.46	4.97
WS_2 @400 nm	30	20				2.24 ± 0.112		18.667	10.08		10.08
	50	33	RSA	33.5 ± 1.16		4.06 ± 0.203	279.167	33.833	18.20	4.78	18.82
	100	67	RSA	22.3 ± 1.12		2.79 ± 0.139	185.833	23.250	12.50	3.18	12.91
	280	188	RSA	11.3 ± 0.57		1.42 ± 0.071	94.167	11.833	6.36	1.61	6.56
Ni-WS_2 @400 nm	30	20	SA + RSA	53.2 ± 2.66	0.10 ± 0.005	3.16 ± 0.158	1773.333	105.333	14.17	7.59	16.07
	50	33	SA + RSA	14.5 ± 0.73	0.45 ± 0.022	2.45 ± 0.122	483.333	81.667	10.98	2.06	11.18
	100	67	SA + RSA	10.3 ± 0.52	0.94 ± 0.047	1.60 ± 0.080	343.333	53.333	7.17	1.47	7.32
	280	188	SA + RSA	0.73 ± 0.04	0.85 ± 0.042	0.75 ± 0.037	24.333	25.000	3.36	0.10	0.36

Table 2
Literature review for NLO parameters of different WS_2 samples.

Samples	Excitation details	NLO process	β(cm/GW)	I_{sat}(kW/cm^2)	n_2(cm^2/W)	α_0 (cm^{-1})	Ref.
WS_2 thin films	He–Ne (632.8 nm)	TPA (RSA)	10^{10} (β < 0)	1.3–0.214		1.38×10^5 - 2.52×10^5	[32]
	Diode laser (655 nm)		10^{10} (β > 0)	5.28–3.8	–	1.37×10^5 - 2.54×10^5	
WS_2	800 nm, 130 fs,1 kHz	RSA	18.29 to 0.63	–	–	~3.34×10^{-4}	[57]
WS_2 dispersion	800 nm	SA	-1.8×10^{-4}	–	–	5.0–1.9	[58]
	35 fs, 1 kHz		-1.0×10^{-2}				
WS_2 film		RSA	−92.0 to −22.0	–	–	361–310	
WS_2 nanoflakes	532 nm	Thermo-optical coefficients	12.79×10^9	–	1.5×10^{-4}	68.9	[59]
	CW laser						
	100 mW						
WS_2 films	1030 nm (340 fs)	TPA	1.0×10^4	26	–	7.17×10^5	[45]
	800 nm, (40 fs), 1 kHz	TPA	525	–		1.08×10^6	
	515 nm (340 fs)	SA	-2.9×10^4	–		5.18×10^6	
WS_2	800 nm	TPA	37×10^4	–	8.4×10^{-9}	8.1×10^{-13}	[60]
	1 kHz						
	100 fs						
WS_2 nanosheets	1064 nm,	TPA	31.2	0.060	71.5×10^{-10}	–	[34]
Trigonal prismatic phase	4 ns, 1–10 Hz	SA	131.1	0.075			
	532 nm				4.24×10^{-12}		
	4 ns, 1–10 Hz						
WS_2 nanosheets	532 nm	TPA	1.42	930	–	–	[61]
	10 ns						
WS_2 thin film	632.8 nm	TPA	1.73×10^{10}	–	1.1×10^{-4}	–	[62]
	CW						
WS_2	1060 nm	SA	-0.41×10^4	3150		0.90×10^4	[63]
	175 fs						
WS_2 nanosheets	532 nm,	SA	3×10^{-4}	–	–	–	[56]
	500 nJ, 175 fs	RSA	1.2	–	–	–	
WS_2 film	800 nm	TPA	β = 63.86 cm/GW				[64]
	190 fs	SA	β = −97.59 cm/GW (at sputtering time for for 1 h)				
	1 kHz		β = −62.75 cm/GW (at substrate temperature for 250 °C)				
	500 nJ		β = 389.9 cm/GW (at substrate temperature for 350 °C)				
WS_2 solutions	800 nm	TPA	4.49×10^{-2}		1.62×10^{-15}		This
	400 nm	RSA	33.5×10^{-2}		3.9×10^{-15}		Study
Ni-WS_2 solutions	800 nm	TPA + SA	5.58×10^{-2}	11.2×10^8	1.47×10^{-15}		This
	400 nm	SA + RSA	53.2×10^{-2}	0.10×10^8	3.74×10^{-15}		Study

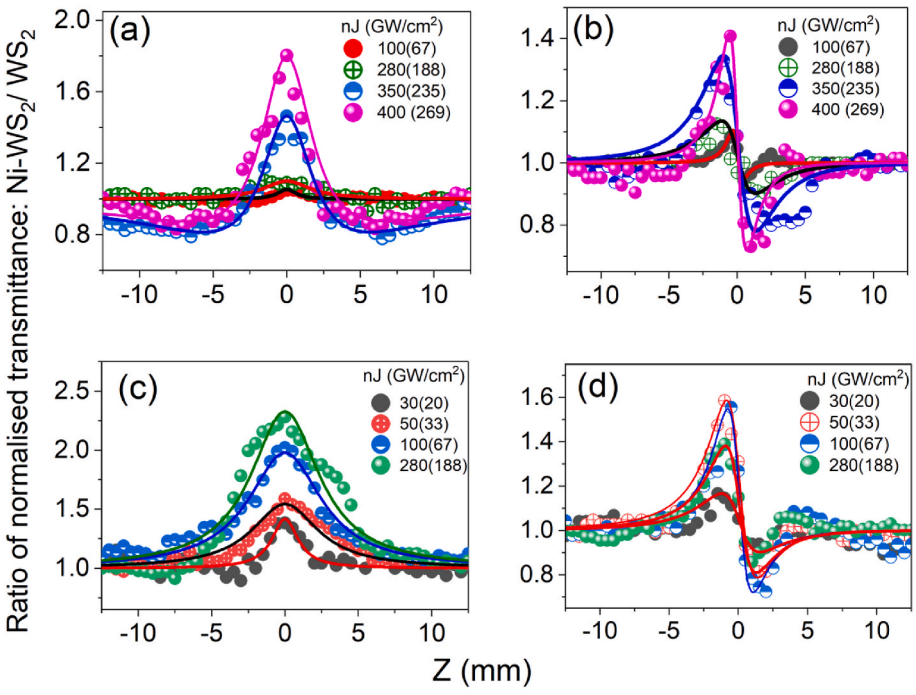

Fig. 5. The ratio of Z-scans at excitation wavelength (a, b) 800 nm, (c,d) 400 nm for Ni-WS_2 with respect to pure WS_2 in the case of (a,c) open-aperture and (b, d) closed-aperture measurements. The solid lines are theoretical fits while the symbols represent the experimental data.

transmittance with respect Ni-WS_2 to pure WS_2.

Table 2 shows the comparison of reported third order NLO parameters for various WS_2 samples. One can see that the NLO parameters of these species significantly affected by excitation wavelength. As shown in Ref. [56], in case of WS_2 nanosheets, the obtained β values are two orders higher than in the present case. Zhou et al. [56] measured the NLO parameters for at 532 nm, 500 nJ, 175 fs, but in the present case we have used the 400 and 800 nm, 60 fs pulses. In the present case, the measured β values for Ni-WS_2 were higher than those for WS_2 in the case of 800 nm pump wavelength. Moreover, Ni-WS_2 depicts an additional process (SA). The I_{sat} values are decreased with an increase of the input laser intensity. This indicates that the materials transmitted a larger portion of input laser pulse. Thus, these 2D TMC materials can be used for optical limiting/switching applications. Additionally, these samples can be used for optical communications/sensing applications since their nonlinearities can be tuned by adding NiO NPs.

It was observed that the nonlinear absorption coefficients are approximately one order of magnitude higher in the case of 400 nm excitation compared with 800 nm excitation. In the case of 400 nm pulses, the higher nonlinear absorbance was achieved for pure WS_2 than in the case of 800 nm pulses due to the influence of the broad absorption band near 400 nm. This leads to the resonance-induced growth of RSA at 400 nm compared to 800 nm. The excitation of WS_2 few-layer nanosheets at 400 nm under these resonance-induced circumstances can strengthen the third-order susceptibilities due to contribution from different resonances [65]. Also, the formation of hot electrons could influence variations in the nonlinear refraction at resonance-induced conditions [66]. Hence, the nonlinear refractive index of pristine WS_2 at $\lambda = 400$ nm was higher than at the non-resonant wavelength (800 nm).

However, we have further made an analysis of Z-scan data obtained from OA and CA measurements (Figs. 3 and 4) by considering the ratio of normalized transmittance for Ni-WS_2 to pure WS_2. Fig. 5 presents the ratios of the normalized transmittances from Ni-WS_2 and WS_2 to verify the nonlinear absorption and refraction attributed to Ni dopants at the excitation wavelengths of 800 and 400 nm. The obtained ratio curves are well fitted with equations (2) and (3) for OA cases, describing the SA and TPA + SA, and equation (4) shows NRA process with self-defocusing effect. In the case of both excitation wavelengths the NiO NP dopants show SA [Fig. 5(a and b)] and self-defocusing effect [Fig. 5(c and d)] with variation on input laser pulse energies.

In the case of 800 nm, at the laser input energies 100, 280, 350, and 400 nJ (67, 188, 235, and 269 GW/cm^2), Ni dopants depicted saturation intensities 70.8, 94.5, 6.02 and 6.4 × 10^{10} W/cm^2 and n_2 values −7.09, −3.89, −7.46, −8.09 (× 10^{-16}) cm^2/W, respectively. Also, at 350 and 400 nJ pulse energies Ni dopants show TPA and corresponding β values are 8.4 and 6.8 × 10^{-11} cm/W, respectively. At higher pulse energy 400 nJ the β decreased and increased the saturation intensity compared to values obtained at 350 nJ pulse energy. Meanwhile, in the case of 400 nm, at the laser input energies 30, 50, 100, and 280 nJ (20, 33, 67, and 188 GW/cm^2), Ni dopants depicted saturation intensities of 4.84, 6.19, 6.88 and 14.2 × 10^{10} W/cm^2 and n_2 fraction processes for Ni dopants corroborate with our earlier reported work at 400 nm [67] and at 800 nm [68], wherein we demonstrated the contribution of Ni dopants (average size of 20 nm) in the case of $CsPbBr_3$ 2D nanocrystals.

Fig. 6(a,c) and 6(b,d) illustrate the proposed energy level diagram associated with nonlinear absorption processes for WS_2 and Ni-WS_2 at the pump wavelengths 800 nm (photon energy 1.55 eV) and 400 nm (photon energy 3.1 eV), respectively. It was confirmed that the bandgaps of WS_2 and Ni-WS_2 were 1.63 eV and 1.77 eV, respectively [Fig. 2(b)]. In brief, Fig. 6(a) depicts that, at pump wavelength 800 nm and pump energy 280 nJ WS_2 possesses only one possible nonlinear absorption (NLA) mechanism, which is TPA (excitation via the virtual levels). At 350 and 400 nJ, similar TPA curves were observed (see OA Z-scan data, Fig. 3(a)), and one can expect that these excitations processes again realize via the virtual levels. Higher peak intensities resulted in populating the higher states in the conduction band (CB). Fig. 6(b) shows the excitation at the pump wavelength of 400 nm and the only possible NLA mechanism is RSA via lower CB states (real states now) into the deeper states of CB for the pump energies in the range of 30–280 nJ.

As shown in Fig. 3(c), at higher peak intensities, the OA Z-scans shows 'W'-like shape for Ni-WS_2 nanosheets under 800 nm laser excitation. The obtained nonlinear absorption process is further explained based on the energy level diagram. Fig. 6(c) depicts the energy level diagram and possible excitations in the case of NiO-doped WS_2 at 800 nm. The following NLA scenarios can occur at different pulse energies. For the case of 100 nJ pulse energy, due to the presence of defect states and the relatively lower peak intensities, only SA occurs. At 280 nJ (i.e.,

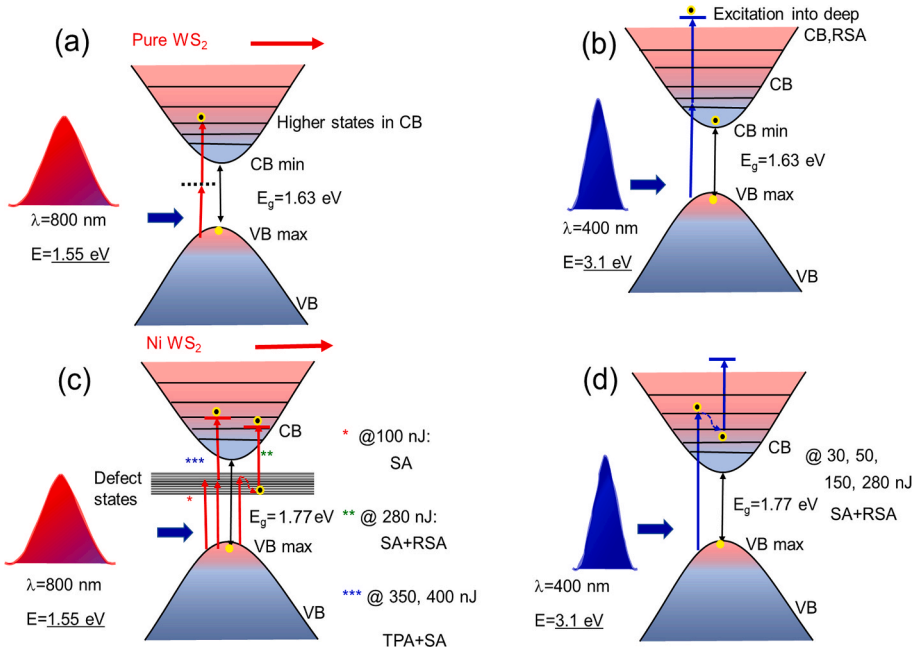

Fig. 6. Energy level diagrams describing the nonlinear absorption processes in (a,b) WS_2 and (c,d) Ni-WS_2 at the pump wavelengths of (a,c) 800 nm and (b,d) 400 nm. VB: valence band, CB: conduction band. 800 nm photon has 1.55 eV energy and 400 nm photon has 3.1eV energy.

at higher peak intensities), there could be the involvement of the transitions from the defect states (arising from the doping) to the CB, leading to RSA (SA at lower peak intensities and RSA at higher peak intensities in the same Z-scan data). In the case of even higher energies (i.e., at 350 and 400 nJ), one can observe the influence of TPA and the saturation of TPA alongside the growing SA, respectively. The former processes can arise due to the stronger excitation of the CB leading to SA at very high peak intensities. The role of RSA in that case can be decreased with regard to TPA, though it is difficult to determine the ratio of these two processes at the discussed conditions.

Fig. 6(d) depicts the NLA processes in Ni-WS_2 at 400 nm. At all pulse energies (30, 50, 150, and 280 nJ) the photon energy (3.1 eV) results in directly populating the CB. Therefore, one can expect a joint presence of SA and RSA. SA occurs at lower peak intensities whereas RSA becomes stronger at higher peak intensities due to possible transitions from lower CB states to the higher CB states. Our experimental data (Fig. 3) followed this pattern of the dynamics of NLA processes.

A recent study [69] discovered an unusual switching behavior from RSA to SA in quasi-2D perovskite film [(PEA)2FAPb2I7]. This transition of NLA processes was achieved at a low intensity (~2.6 GW/cm^2). They argue that this anomalous switching of nonlinear absorption processes was due to (a) ultrafast (<100 fs) non-thermalized carrier induced bleaching effect and (b) many-body effects encouraged above band-edge absorption enrichment. They also pointed out that these mechanisms will be useful in devising the high-speed and low-powered NLO devices. They reported a NLA coefficient of 12.75 cm/MW at 540 nm for the studied quasi-2D perovskite film. In the present studies, we observed this switching in the case of Ni-WS_2 at ~300 nJ corresponding to ~200 GW/cm^2 at 800 nm [Fig. 3(c)]. However, there is scope for improving this threshold by carefully manipulating the amount of doping and the dopant itself. Further, we observed a maximum NLA coefficient of 5.32 $\times 10^{-4}$ cm/MW at 400 nm, which is reasonable since our measurements were in the liquid phase whereas the measurements reported in Ref. [69] were in the film form (the density of the nanoparticles is expected to be much higher in that case). Similar NLA behavior was observed in WS_2 nanoplates dispersion [45] obtained using nanosecond excitation (at wavelengths of 532 nm and 1064 nm). The authors in this case observed NLA coefficients of WS_2 dispersions to be ~10^{-10} m/W. This is again expected since with nanosecond pulses excited state absorption will be dominant nonlinear absorption mechanism leading to higher magnitudes of the effective NLA coefficient. We firmly believe that the broadband NLO coefficients of the investigated WS_2 dispersions in the present case provide a deeper understanding of the nonlinear absorption mechanisms in such 2D materials providing ways to control, improvise, and improve the coefficients for various device performances.

4. Conclusions

In conclusion, we successfully synthesized the WS_2 nanolayers and NiO NPs decorated WS_2 few layers. We determined the bandgaps of the materials and the phase and crystallinity of samples. The Ni NPs in WS_2 layers showed considerable changes of the nonlinear absorptive properties compared with pristine WS_2 nanolayers. In the case of Ni-WS_2 at lower intensities of probe pulses, the SA conquers over the TPA at 800 nm and RSA at 400 nm. With the increase of intensity, the rivalry among these two processes modifies the relative role of SA, TPA, and RSA. In the case of 400 nm pulses, SA overpasses by RSA, while in the case of 800 nm pulses, TPA (and probably RSA) starts playing an important role. Meanwhile, insignificant changes were observed in the negative nonlinear refraction. Thus, the embedded Ni NPs play a crucial role in the nonlinear absorption mechanism of WS_2. This property can be useful for various optical applications such as saturable absorbers for optical devices (limiters/switches).

Authors agreement

I, as a Corresponding author, have submitted this manuscript to Optical materials. All the Co-authors have reviewed and agreed for the submission. Also, there is no conflict of interest.

Dr. Srinivasa Rao Konda

CRediT authorship contribution statement

Srinivasa Rao Konda: Conceptualization, Methodology, Investigation, Validation, Formal analysis, Data curation, Writing – original draft, Writing – review & editing, Visualization. **Rahul A. Rajan:** Investigation, Formal analysis, Data curation, Validation, Writing - original draft. **Subhash Singh:** Methodology, Investigation, Resources, Writing – original draft. **Rashid A. Ganeev:** Conceptualization, Validation, Writing – original draft, Writing – review & editing. **Venugopal Rao Soma:** Conceptualization, Methodology, Validation, Writing – original draft, Writing – review & editing, Visualization. **Amit Srivastava:** Investigation, Resources, Formal analysis. **Mottamchetty Venkatesh:** Formal analysis, Investigation. **Chunlei Guo:** Resources, Validation, Supervision. **Wei Li:** Validation, Writing – review & editing, Supervision, Project administration, Funding acquisition.

Declaration of competing interest

The authors declare that they have no known competing financial interests or personal relationships that could have appeared to influence the work reported in this paper.

Data availability

Data will be made available on request.

Acknowledgements

This work is supported by National Natural Science Foundation of China (grant nos. 62134009, 62121005), the Chinese Academy of Sciences President's International Fellowship Initiative (2021PM0036, 2022VMA0012), The Innovation Grant of Changchun Institute of Optics, Fine Mechanics and Physics (CIOMP), Jilin Provincial Science and Technology Development Project (YDZJ202102CXJD002), Development Program of the Science and Technology of Jilin Province (20200802001GH) and European Regional Development Fund (1.1.1.5/19/A/003). Venugopal Rao Soma thanks DRDO for financial support throug ACRHEM.

References

[1] Y. Cheng, H. Yang, B. Xu, H. Xu, Z. Cai, Passive Q-switching of a diode-pumped Pr : $LiYF_4$ visible laser using WS_2 as saturable absorber, IEEE Photon. J. 8 (2016) 1–6.
[2] M. Nie, B. Li, K. Jia, et al., Dissipative soliton generation and real-time dynamics in microresonator-filtered fiber lasers, Light. Sci. Appl 11 (2022) 296, https://doi.org/10.1038/s41377-022-00998-z.
[3] J. Mohanraj, V. Velmurugan, S. Sivabalan, Transition metal dichalcogenides based saturable absorbers for pulsed, Opt. Mater. 60 (2016) 601–617, https://doi.org/10.1016/j.optmat.2016.09.007.
[4] T. Jiang, K. Yin, J. You, H. Ouyang, Ultrafast fiber lasers mode-locked by two-dimensional materials : review and prospect. https://doi.org/10.1364/PRJ.8.000078, 2020.
[5] Z. Luo, D. Wu, B. Xu, H. Xu, Z. Cai, J. Peng, J. Weng, S. Xu, C. Zhu, F. Wang, Z. Sun, H. Zhang, Two-dimensional material-based saturable absorbers: towards compact visible-wavelength all-fiber pulsed lasers, Nanoscale 8 (2016) 1066–1072, https://doi.org/10.1039/c5nr06981e.
[6] C. Tan, X. Cao, X. Wu, Q. He, J. Yang, X. Zhang, J. Chen, W. Zhao, S. Han, G. Nam, M. Sindoro, H. Zhang, Recent advances in ultrathin two-dimensional nanomaterials, Chem. Rev. 117 (2017) 6225–6331, https://doi.org/10.1021/acs.chemrev.6b00558.
[7] P. Zhang, F. Wang, Two-dimensional materials for miniaturized energy storage devices : from individual devices to smart integrated systems, Chem. Soc. Rev. 47 (2018) 7426–7451, https://doi.org/10.1039/c8cs00561c.

[8] X. Chia, M. Pumera, Dimensional materials for electrocatalysis, Nat. Catal. 1 (2018) 909–921, https://doi.org/10.1038/s41929-018-0181-7.

[9] X. Wu, H. Zhang, J. Zhang, X. Wen, D. Lou, Recent advances on transition metal dichalcogenides for electrochemical energy conversion, Adv. Mater. 2008376 (2021) 1–24, https://doi.org/10.1002/adma.202008376.

[10] P. You, et al., 2D materials for conducting holes from grain boundaries in perovskite solar cells, Light: Science & Applications 10 (2021) 695–706, https://doi.org/10.1038/s41377-021-00515-8.

[11] H.S. Kang, S. Yang, Photopatterning via photofluidization of azobenzene polymers [J], Light: Advanced Manufacturing 3 (2022) 3, https://doi.org/10.37188/lam.2022.003.

[12] S. Bai, and K. Sugioka, Recent advances in the fabrication of highly sensitive surface-enhanced raman scattering substrates: nanomolar to attomolar level sensing[J], Light: Adv. Manufact. 2 (2021) 13, doi:10.37188/lam.2021.013.

[13] D. Lee, S. So, G. Hu, et al., Hyperbolic metamaterials: fusing artificial structures to natural 2D materials, eLight 2 (2022) 1, https://doi.org/10.1186/s43593-021-00008-6.

[14] G. Huang, Y. Liu, D. Wang, et al., Upconversion nanoparticles for super-resolution quantification of single small extracellular vesicles, eLight 2 (2022) 20, https://doi.org/10.1186/s43593-022-00031-1.

[15] Z. Guo, Y. Zeng, F. Meng, et al., In-situ neutron-transmutation for substitutional doping in 2D layered indium selenide based phototransistor, eLight 2 (2022) 9, https://doi.org/10.1186/s43593-022-00017-z.

[16] L. Yang, F. Mayer, U.H. Bunz, E. Blasco, M. Wegener, Multi-material multi-photon 3D laser micro- and nanoprinting[J], Light: Adv. Manufact. 2 (2021) 17, https://doi.org/10.37188/lam.2021.017.

[17] J. Zhang, L. Du, S. Feng, R.W. Zhang, B. Cao, C. Zou, Y. Chen, M. Liao, B. Zhang, S. A. Yang, G. Zhang, T. Yu, Enhancing and controlling valley magnetic response in MoS_2/WS_2 heterostructures by all-optical route, Nat. Commun. 10 (2019) 1–9, https://doi.org/10.1038/s41467-019-12128-2.

[18] G. Li, X. Yang, L. Li, H. Zhang, Z. Zhang, Passively Q-switched Tm : YAP laser with a WSe_2 saturable absorber passively Q-switched Tm : YAP laser with a WSe_2 saturable absorber, IOP Conf. Ser. Mater. Sci. Eng. 782 (2020), 022106, https://doi.org/10.1088/1757-899X/782/2/022106.

[19] E.T. Poh, S.X. Lim, C.H. Sow. Multifaceted Approaches to Engineer Fluorescence in Nanomaterials via a Focused Laser Beam[J], Light: Advanced Manufacturing 3 (2022) 4, doi:10.37188/lam.2022.004.

[20] J.H. Chen, Y.F. Xiong, F. Xu, et al., Silica optical fiber integrated with two-dimensional materials: towards opto-electro-mechanical technology, Light. Sci. Appl. 10 (2021) 78, https://doi.org/10.1038/s41377-021-00520-x.

[21] S. Guo, S. Jin, E. Park, L. Chen, L. Guo, Y.M. Jung, Enhanced surface-enhanced Raman scattering activity of MoS_2−Ag-reduced graphene oxide : structure-mediated excitonic transition, J. Phys. Chem. C 125 (2021) 23259–23266, https://doi.org/10.1021/acs.jpcc.1c06387.

[22] N. Ansari, E. Mohebbi, K. Mirbaghestan, Tunable dual-wavelength saturable absorber based on dual defective photonic crystal by MoS_2 monolayer Narges, Photon. Nanostruct: Fundam. Appl. (2021), 100976, https://doi.org/10.1016/j.photonics.2021.100976.

[23] H. Liu, C. Yao, C. Jiang, X. Wang, Preparation , modification and nonlinear optical properties of semiconducting MoS_2 and MoS_2/ZnO composite film, Opt Laser. Technol. 138 (2021), 106905, https://doi.org/10.1016/j.optlastec.2020.106905.

[24] M. Balaei, R. Karimzadeh, H. Saghaei, S. Ghayeb-Zamharir, The effect of laser wavelength and concentration on the optical limiting response of exfoliated MoS_2 in the NMP solvent, Eur. Phys. J. Plus. 136 (2021), https://doi.org/10.1140/epjp/s13360-021-01259-5.

[25] Z. Dehghani, F. Ostovari, M. Nadafan, Investigation of the structural, dielectric, and optical properties of $MoSe_2$ nanosheets, J. Appl. Phys. 131 (2022), 213101, https://doi.org/10.1063/5.0088016.

[26] F. Zha, H. Chu, Z. Pan, H. Pan, S. Zhao, M. Yang, D. Li, Large-scale few-layered MoS_2 as a saturable absorber for Q-switching operation at 2.3 μm, Opt. Lett. 47 (2022) 3271, https://doi.org/10.1364/ol.462325.

[27] T. Liu, Q. Liu, R. Hong, Y. Shi, C. Tao, Q. Wang, H. Lin, Z. Han, D. Zhang, Cu_2O induced the enhancement of nonlinear absorption of MoS_2 thin film, J. Alloys Compd. 886 (2021), https://doi.org/10.1016/j.jallcom.2021.161137.

[28] J. Wang, H. Li, Y. Ma, M. Zhao, W. Liu, B. Wang, S. Wu, X. Liu, L. Shi, T. Jiang, J. Zi, Routing valley exciton emission of a WS_2 monolayer via delocalized Bloch modes of in-plane inversion-symmetry-broken photonic crystal slabs, Light Sci. Appl. 9 (2020), https://doi.org/10.1038/s41377-020-00387-4.

[29] J. Hui Chen, J. Tan, G. Xing Wu, X. Jin Zhang, F. Xu, Y. Qing Lu, Tunable and enhanced light emission in hybrid WS_2-optical-fiber-nanowire structures, Light Sci. Appl. 8 (2019), https://doi.org/10.1038/s41377-018-0115-9, 0–7.

[30] J. Xiao, Z. Ye, Y. Wang, H. Zhu, Y. Wang, X. Zhang, Nonlinear optical selection rule based on valley-exciton locking in monolayer ws_2, Light Sci. Appl. 4 (2015) 1–6, https://doi.org/10.1038/LSA.2015.139.

[31] G.Q. Jiang, C.B. Yao, Z.M. Wang, X. Wang, Y. Cai, Semiconducting ZnO & WS_2 heterojunction composite films: fabrication, characterization and ultrafast nonlinear properties, J. Alloys Compd. 863 (2021), 158664, https://doi.org/10.1016/j.jallcom.2021.158664.

[32] S. Abutalebi bagherabad, M. Khanzadeh, S.M. Marashi, Laser beam intensity and wavelength dependent nonlinear absorption in pulse laser deposited WS_2 thin films, Opt. Mater. 127 (2022), 112249, https://doi.org/10.1016/j.optmat.2022.112249.

[33] G. Jiang, C. Yao, S. Bao, Y. Cai, Standing growth mechanism and ultrafast nonlinear absorption properties of WS_2 films, Opt. Mater. 106 (2020), 109995, https://doi.org/10.1016/j.optmat.2020.109995.

[34] M. Stavrou, N. Chazapis, E. Nikoli, R. Arenal, N. Tagmatarchis, S. Couris, Crystalline phase effects on the nonlinear optical response of MoS_2 and WS_2 Nanosheets: implications for photonic and optoelectronic applications, ACS Appl. Nano Mater. (2022), https://doi.org/10.1021/acsanm.2c03709.

[35] P. Qi, Y. Luo, B. Shi, et al., Phonon scattering and exciton localization: molding exciton flux in two dimensional disorder energy landscape, eLight 1 (2021) 6, https://doi.org/10.1186/s43593-021-00006-8.

[36] B. Lai, S.C. Singh, J.K. Bindra, C.S. Saraj, A. Shukla, T.P. Yadav, W. Wu, S. A. McGill, N.S. Dalal, A. Srivastava, C. Guo, Hydrogen evolution reaction from bare and surface-functionalized few-layered MoS_2 nanosheets in acidic and alkaline electrolytes, Mater, Today Chem 14 (2019), https://doi.org/10.1016/j.mtchem.2019.100207.

[37] A. Brasington, D. Golla, A. Dave, B. Chen, S. Tongay, J. Schaibley, B.J. LeRoy, A. Sandhu, Role of defects and phonons in bandgap dynamics of monolayer WS_2 at high carrier densities, JPhys Mater 4 (2021), https://doi.org/10.1088/2515-7639/abc13b.

[38] B. Zhu, X. Chen, X. Cui, Exciton binding energy of monolayer WS_2, Sci. Rep. 5 (2015) 1–5, https://doi.org/10.1038/srep09218.

[39] J. Kopaczek, M.P. Polak, P. Scharoch, K. Wu, B. Chen, S. Tongay, R. Kudrawiec, Direct optical transitions at K- and H-point of Brillouin zone in bulk MoS_2, $MoSe_2$, WS_2, and WSe_2, J. Appl. Phys. 119 (2016), https://doi.org/10.1063/1.4954157.

[40] P. H.T, G.E. Weijie Zhao, Zohreh Ghorannevis, Leiqiang Chu, Minglin Toh, Christian Kloc, Evolution ofElectronic Structure in Atomically Thin Sheets of WS_2 and WSe_2, ACS Nano (2013) 791–797.

[41] H. Song, X. Yu, M. Chen, M. Qiao, T. Wang, J. Zhang, Y. Liu, P. Liu, X. Wang, Modification of WS_2 nanosheets with controllable layers via oxygen ion irradiation, Appl. Surf. Sci. 439 (2018) 240–245, https://doi.org/10.1016/j.apsusc.2018.01.019.

[42] N. Li, J. Su, Z. Xu, D.-P. Li, Z.-T. Liu, Theoretical and experimental investigation on structural and electronic properties of Al/O/Al, O-doped WS_2, J. Phys. Chem. Solid. 89 (2016) 84–88, https://doi.org/10.1016/j.jpcs.2015.10.016.

[43] L.Y. Xie, J.M. Zhang, Electronic structures and magnetic properties of the transition-metal atoms (Mn, Fe, Co and Ni) doped WS_2: a first-principles study, Superlattice. Microst. 98 (2016) 148–157, https://doi.org/10.1016/j.spmi.2016.08.015.

[44] Y.Q. Qin, Y.Q. Peng, W.F. Yang, Y. Wang, J.W. Cui, Y. Zhang, Ultrathin exfoliated WS_2 nanosheets in low-boiling-point solvents for high-efficiency hydrogen evolution reaction, IOP Conf. Ser. Mater. Sci. Eng. 770 (2020), https://doi.org/10.1088/1757-899X/770/1/012079.

[45] S. Zhang, N. Dong, N. McEvoy, M. Obrien, S. Winters, N.C. Berner, C. Yim, Y. Li, X. Zhang, Z. Chen, L. Zhang, G.S. Duesberg, J. Wang, Direct observation of degenerate two-photon absorption and its saturation in WS_2 and MoS_2 monolayer and few-layer films, ACS Nano 9 (2015) 7142–7150, https://doi.org/10.1021/acsnano.5b03480.

[46] X. Gu, R. Yang, Phonon transport in single-layer transition metal dichalcogenides: a first-principles study, Appl. Phys. Lett. 105 (2014), https://doi.org/10.1063/1.4896685.

[47] Z. Zhang, Y. Xie, Y. Ouyang, Y. Chen, A systematic investigation of thermal conductivities of transition metal dichalcogenides, Int. J. Heat Mass Tran. 108 (2017) 417–422, https://doi.org/10.1016/j.ijheatmasstransfer.2016.12.041.

[48] I.H. Chowdhury, X. Xu, Heat transfer in femtosecond laser processing of metal, Numer. Heat Tran. 44 (2003) 219–232, https://doi.org/10.1080/716100504.

[49] G. N, K. Kalli, K. Sugde, Advances in femtosecond micromachining and inscription of micro and nano photonic devices, Front. Guid. Wave Opt. Optoelectron. (2010), https://doi.org/10.5772/39542.

[50] T. Kramer, S. Remund, B. Jäggi, M. Schmid, B. Neuenschwander, Ablation dynamics-from absorption to heat accumulation/ultra-fast laser matter interaction, Adv. Opt. Technol. 7 (2018) 129–144, https://doi.org/10.1515/aot-2018-0010.

[51] G. Raciukaitis, M. Brikas, P. Gecys, M. Gedvilas, Accumulation effects in laser ablation of metals with high-repetition-rate lasers, High-Power Laser Ablation VII 7005 (2008), 70052L, https://doi.org/10.1117/12.782937.

[52] P.B. Chapple, J. Staromlynska, J.A. Hermann, T.J. Mckay, R.G. Mcduff, Single-beam Z-scan: measurement techniques and analysis, J. Nonlinear Opt. Phys. Mater. 6 (1997) 251–293, https://doi.org/10.1142/S0218863597000204.

[53] X. Liu, S. Guo, H. Wang, L. Hou, Theoretical study on the closed-aperture Z-scan curves in the materials with nonlinear refraction and strong nonlinear absorption, Opt Commun. 197 (2001) 431–437, https://doi.org/10.1016/S0030-4018(01)01406-7.

[54] R.A. Ganeev, K.S. Rao, Z. Yu, W. Yu, C. Yao, Y. Fu, K. Zhang, C. Guo, Strong nonlinear absorption in perovskite films, Opt. Mater. Express 8 (2018) 1472–1483, https://doi.org/10.1364/OME.8.001472.

[55] R.A. Ganeev, V.S. Popov, A.I. Zvyagin, N.A. Lavrentyev, A.E. Mirofyanchenko, E. V. Mirofyanchenko, I.A. Shuklov, O.V. Ovchinnikov, V.P. Ponomarenko, V. F. Razumov, Exfoliated Bi_2Te_3 nanoparticle suspensions and fi lms : morphological and nonlinear optical characterization, Nanophotonics 10 (2021) 3857–3870.

[56] K.G. Zhou, M. Zhao, M.J. Chang, Q. Wang, X.Z. Wu, Y. Song, H.L. Zhang, Size-dependent nonlinear optical properties of atomically thin transition metal dichalcogenide nanosheets, Small 11 (2015) 694–701, https://doi.org/10.1002/smll.201400541.

[57] R. Wei, X. Tian, H. Zhang, Z. Hu, X. He, Z. Chen, Q. Chen, J. Qiu, Facile synthesis of two-dimensional WS_2 with reverse saturable absorption and nonlinear refraction properties in the PMMA matrix, J. Alloys Compd. 684 (2016) 224–229, https://doi.org/10.1016/j.jallcom.2016.05.169.

[58] C. Lu, D. Yang, J. Ma, M. Luo, Y. Jin, X. Xu, Effect of surface oxidation on nonlinear optical absorption in WS_2 nanosheets, Appl. Surf. Sci. 532 (2020), 147409, https://doi.org/10.1016/j.apsusc.2020.147409.

[59] Z. Mahmudi, S.Z. Mortazavi, A. Reyhani, A. Taherkhani, P. Parvin, Non-linear thermo-optical properties of WS_2 and Au/WS_2 Schottky-type nano/hetero-junctions, Mater. Sci. Eng. B Solid-State Mater. Adv. Technol. 283 (2022), 115814, https://doi.org/10.1016/j.mseb.2022.115814.

[60] X. Zheng, Y. Zhang, R. Chen, X. Cheng, Z. Xu, T. Jiang, Z-scan measurement of the nonlinear refractive index of monolayer WS_2, Opt Express 23 (2015), 15616, https://doi.org/10.1364/oe.23.015616.

[61] S. Karmakar, U. Chatterjee, P. Kumbhakar, Transition from saturable absorption to reverse saturable absorption in multi-layered WS_2 nanosheets, Opt Laser. Technol. 136 (2021), 106696, https://doi.org/10.1016/j.optlastec.2020.106696.

[62] G. Pradhan, A.K. Sharma, Linear and nonlinear optical response of sulfur-deficient nanocrystallite WS_2 thin films, J. Mater. Sci. 54 (2019) 14809–14824, https://doi.org/10.1007/s10853-019-03986-8.

[63] Z. Du, C. Zhang, M. Wang, X. Zhang, J. Ning, X. Lv, G. Zhao, Z. Xie, J. Xu, S. Zhu, Synthesis of $WS_{1.76}Te_{0.24}$ alloy through chemical vapor transport and its high-performance saturable absorption, Sci. Rep. 9 (2019) 1–9, https://doi.org/10.1038/s41598-019-55755-x.

[64] G.Q. Jiang, C.B. Yao, S. Bin Bao, Y. Cai, Standing growth mechanism and ultrafast nonlinear absorption properties of WS_2 films, Opt. Mater. 106 (2020), 109995, https://doi.org/10.1016/j.optmat.2020.109995.

[65] D. Smirnova, Y.S. Kivshar, Multipolar nonlinear nanophotonics, Optica 3 (2016) 1241, https://doi.org/10.1364/optica.3.001241.

[66] Y. Guillet, M. Rashidi-Huyeh, B. Palpant, Influence of laser pulse characteristics on the hot electron contribution to the third-order nonlinear optical response of gold nanoparticles, Phys. Rev. B Condens. Matter 79 (2009) 1–9, https://doi.org/10.1103/PhysRevB.79.045410.

[67] S.R. Konda, V.R. Soma, R.A. Ganeev, M. Banavoth, R. Ketavath, W. Li, Third-order optical nonlinearities and high-order harmonics generation in Ni-doped $CsPbBr_3$ nanocrystals using single- and two-color chirped pulses, J. Mater. Sci. 57 (2022) 3468–3485, https://doi.org/10.1007/s10853-022-06871-z.

[68] S.R. Konda, R.A. Ganeev, V.V. Kim, High-order harmonics generation in nanosecond-pulses-induced plasma containing Ni-doped $CsPbBr_3$ perovskite nanocrystals using chirp-free and chirped femtosecond pulses, Nanotechnology 34 (2023), 055705.

[69] G. Wang, T. Liu, B. Wang, H. Gu, Q. Wei, Z. Zhang, J. He, M. Li, G. Xing, Hot-carrier tunable abnormal nonlinear absorption conversion in quasi-2D perovskite, Nat. Commun. 13 (2022) 6935, https://doi.org/10.1038/s41467-022-34705-8.